Heliyon 10 (2024) e38721

Contents lists available at ScienceDirect

Heliyon

journal homepage: www.cell.com/heliyon

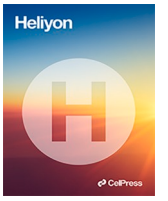

Research article

# Facile one-pot synthesis of $CuO–Bi_2O_3/MgAl_2O_4$ catalyst and its performance in the ethynylation of formaldehyde

Gang Guan [a], Fengyun Ma [a,*], Ping Luo [b,c,**], Xiaolin Zhang [b,c], Xiaoding Li [b,c], Guangxing Li [d,***]

[a] College of Chemistry and Chemical Engineering, Xinjiang University, Urumqi, Xinjiang, 830046, PR China
[b] Hubei Research Institute of Chemistry, Jianghan University, Wuhan, 430056, PR China
[c] Haiso Technology Co., LTD, Hubei Province, Wuhan, 430020, PR China
[d] School of Chemistry and Chemical Engineering, Huazhong University of Science & Technology, Wuhan, 430074, PR China

ARTICLE INFO

*Keywords:*
$CuO–Bi_2O_3/MgAl_2O_4$ catalyst
$MgAl_2O_4$ support
One-pot synthesis
Ethynylation
1,4-Butynediol

ABSTRACT

The $CuO–Bi_2O_3/MgAl_2O_4$ catalyst was synthesized via one-pot synthesis and used to catalyze formaldehyde (HCHO) ethynylation. Coprecipitation using $Cu^{2+}$, $Bi^{3+}$, $Mg^{2+}$, and $Al^{3+}$ nitrates and NaOH generated Cu and Bi oxides and spinel $MgAl_2O_4$ phase. The catalyst precursor was calcined at 450 °C. The catalytic performance of $CuO–Bi_2O_3/MgAl_2O_4$ in the synthesis of 1,4-butynediol via HCHO ethynylation was investigated. The presence of a new spinel phase enhanced the acid–base properties on the catalyst surface and prevented the aggregation of CuO particles. These properties resulted in improved CuO dispersion during calcination and CuO particle growth suppression, affording smaller CuO crystals. The $MgAl_2O_4$ support facilitated the reduction of $Cu^{2+}$ to $Cu^{+}$ and formation of abundant active species during the reaction. The catalyst exhibited abundant weakly basic, fewer strongly basic, and least acidic sites, which facilitated the adsorption of HCHO and acetylene. The catalytic performance of $CuO–Bi_2O_3/MgAl_2O_4$ demonstrated 97 % conversion and 80 % selectivity after the online monitoring of the ethynylation reaction for 6 h. The leaching of Cu during the reaction, as analyzed by inductively coupled plasma spectroscopy, was extremely low. Moreover, conversion and selectivity did not substantially change after eight cycles. In addition, the catalyst exhibited superior activity and long-term stability in the ethynylation reaction.

## 1. Introduction

The catalytic ethynylation of formaldehyde (HCHO) to 1,4-butynediol (BYD) via the Reppe reaction is a crucial reaction [1–4]. BYD can be hydrogenated to synthesize 1,4-butanediol, an essential raw material for synthesizing high-value chemicals such as 3-butene-1-alcohol, tetrahydrofuran, and poly(tetramethylene ether) glycol [5–10].

$$HC \equiv CH + 2HCHO \rightarrow HOCH_2C \equiv CCH_2OH \quad (1)$$

* Corresponding author.
** Corresponding author. Hubei Research Institute of Chemistry, Jianghan University, Wuhan, 430056, PR China.
*** Corresponding author.
*E-mail addresses:* ma_fy@126.com (F. Ma), lp98311@126.com (P. Luo), ligxabc@163.com (G. Li).

https://doi.org/10.1016/j.heliyon.2024.e38721
Received 12 June 2024; Received in revised form 18 September 2024; Accepted 27 September 2024
Available online 27 September 2024

However, the activity and stability of popular Cu–Bi-based catalysts for ethynylation under a reducing atmosphere in the aldehyde–acetylene ($C_2H_2$) process are of significant concern. Challenges, such as activity and catalyst lifetime, have prompted researchers to explore new catalytic systems for this reaction [5–9]. Therefore, the design and construction of novel and efficient Cu-based catalysts for ethynylation in this pseudo-homogeneous catalytic system is essential to enhance the reaction efficiency. In particular, the optimization of support is crucial.

Catalysts used in the ethynylation process can be divided into two categories: unsupported and supported, with the most common active components being Cu–Bi, Cu–Zn, and Cu–Fe [10–16]. Cu is converted to cuprous acetylide ($Cu_2C_2$ or Cu–C ≡ C–Cu) during the ethynylation reaction [17–20]. The use of supports significantly enhances the performance of these catalysts. Various catalyst supports, including $SiO_2$ [21–23], molecular sieves [24,25], MgO–$SiO_2$ [26,27], MgO–$Al_2O_3$–$SiO_2$ [28], and $Al_2O_3$ [29], have been used for the ethynylation reaction. Although $SiO_2$ and γ-$Al_2O_3$ supports exhibit high specific surface areas and stabilities, their surface acidic sites cause the polymerization of acetylene to form polyacetylene during the formaldehyde ethynylation reaction [16,30].The polyacetylene can block the catalyst pores, cover the active sites, and reduce the catalyst activity. In addition, the presence of vacancies in the γ-$Al_2O_3$ structure makes it structurally unstable, resulting in crystal phase collapse and catalyst inactivation [31,32].

To address the limitations of the γ-$Al_2O_3$ support, researchers introduced MgO into γ-$Al_2O_3$ and synthesized a catalyst with $MgAl_2O_4$ as the support and Cu–Bi as the active component. This catalyst was used for the ethynylation reaction. The incorporation of basic MgO to γ-$Al_2O_3$ altered the acid–base properties of the γ-$Al_2O_3$ surface [27] and filled vacancies in the γ-$Al_2O_3$ lattice with Mg ions. This process generated $MgAl_2O_4$ with a stable spinel structure, thereby addressing the limitations of the γ-$Al_2O_3$ structure [33,34]. $MgAl_2O_4$ exhibits excellent properties such as suitable surface acid–base characteristics, high specific surface area, high melting point, and good wear resistance [35,36]. These properties address the limitations of $Al_2O_3$ and $SiO_2$ supports, thereby improving the activity and stability of the catalyst during reactions. To date, no studies have reported the use of $MgAl_2O_4$ supports for this type of catalyst. Therefore, the efficiency of CuO–$Bi_2O_3$/$MgAl_2O_4$ catalyst in the ethynylation reaction must be investigated. In addition, elucidating the interactions between the $MgAl_2O_4$ support and active components is crucial.

The CuO–$Bi_2O_3$/$MgAl_2O_4$ catalyst was synthesized via a facile one-pot synthesis involving the neutralization of Cu, Bi, Mg, and Al nitrates by NaOH solution, followed by the calcination of the resulting precipitate at approximately 450 °C. The catalysts were characterized using techniques such as X-ray powder diffraction (XRD), hydrogen temperature–programmed reduction ($H_2$-TPR), X-ray photoelectron spectroscopy (XPS), high-resolution transmission electron microscopy (HR-TEM), etc. The effects of MgO content, calcination conditions, and other factors, such as surface acid–base properties, structure, and texture of $MgAl_2O_4$ support were examined. In addition, the effects of these factors on the catalytic activity and stability for the ethynylation reaction were analyzed. Insights into the role of the chemical states of $MgAl_2O_4$ and Mg, as well as the synergistic interactions between the active $Cu^+$ species and basic sites, provide theoretical guidance for the rational design of catalysts for ethynylation reactions.

## 2. Experimental sections

### 2.1. Catalyst preparation

Cu, Bi, Mg, and Al nitrate solutions were mixed with NaOH solution. The reaction temperature, pH, and time were carefully controlled during coprecipitation. Upon completion of the reaction, the catalyst was obtained by washing and drying of the precipitate at 120 °C followed by calcination at 450 °C. Samples with different mass percentages of MgO (0 %, 5 %, 10 %, 15 %, 20 %, and 25 %) are denoted as CB0MA, CB5MA, CB10MA, CB15MA, CB20MA, and CB25MA, respectively. CuO–$Fe_2O_3$/$MgAl_2O_4$ (CF10MA) and CuO/$MgAl_2O_4$ (C10MA) were prepared using the same method as described above. CB10MA was thermally treated in an atmosphere at 250 °C, 350 °C, 450 °C, 550 °C, and 650 °C (heating rate: 3 °C/min) to obtain the CB10MA250, CB10MA350, CB10MA450, CB10MA550, and CB10MA650 catalysts, respectively (see Appendix A for details on catalyst preparation).

### 2.2. Characterization of the catalysts

Brunauer–Emmett–Teller (BET) $N_2$ adsorption–desorption analysis (ASAP 2460, Micromeritics, USA) was used to determine the specific surface area and pore size distribution. Wide-angle XRD (SmartLab SE, Rigaku, Rigaku Co., Ltd., Japan) was used to analyze the crystal structure (2θ = 10°–90°, scan rate = 5°/min). XPS (Scientific K-Alpha, ThermoFisher, USA) spectra were recorded to determine the chemical environment and valence states of the elements. The acidic and basic sites on the catalyst surface were detected by the temperature-programmed desorption of $CO_2$/$NH_3$ ($CO_2$/$NH_3$-TPD, BELCAT II, BELMASS, Japan). $H_2$-TPR (AutoChem1 II 2920, Micromeritics, USA) was used to analyze the reducing ability of the active components and their interactions with the support. The detailed morphologies and elemental distributions of the catalysts were obtained by scanning electron microscopy (SEM, TESCAN MIRA LMS, Czech Republic) and scanning TEM (STEM, Talos F200X, Thermo Fisher, USA). The Cu content in the solution was determined by inductively coupled plasma–optical emission spectroscopy (ICP-OES, Optima 8300, PerkinElmer, USA) to investigate Cu leaching (see Appendix A for details on characterization).

### 2.3. Assessment of the catalytic performance

The HCHO solution was initially added to a self-designed slurry bed reactor, followed by a catalyst with a specific particle size and quality. Subsequently, $C_2H_2$ was introduced, and the reactor was heated until the temperature stabilized at 90 °C. After 6 h, the catalyst and liquid-phase products were recovered by discharge and filtration. The BYD and HCHO contents in the liquid phase were then

analyzed to determine the selectivity and conversion, respectively (Figs. S1 and S2). Detailed procedures are provided in Appendix A.

## 3. Results and discussion

### 3.1. Structure, texture, and morphology of the catalysts

The XRD patterns of the catalysts prepared under different conditions are shown in Fig. 1. The characteristic diffraction peaks of CuO were observed at 2θ = 32.5°, 35.5°, 38.7°, and 48.8° for catalysts with varying MgO contents after calcination at 450 °C (JCPDS 48–1548). As the MgO content increased, the intensity of these diffraction peaks increased, indicating the formation of larger crystals. This effect was particularly noticeable when the MgO content exceeded 15 %, resulting in sharp and intense diffraction peaks (Fig. 1a).

As shown in Fig. 1b, CuO with good crystallinity was formed on the CB10MA catalyst surface at 250 °C. When the calcination temperature exceeded 350 °C, particularly >375 °C, Al and Mg chemically interacted to produce the new $MgAl_2O_4$ phase [37]. As the calcination temperature increased, the crystallinity and size of the CuO crystals increased. $MgAl_2O_4$ was formed at 450 °C (Fig. 1b and c). In addition, as the calcination temperature increased, the intensity of the characteristic diffraction peaks of $MgAl_2O_4$ increased.

However, the size of the CuO crystals did not increase at a calcination temperature of 450 °C. $MgAl_2O_4$ with a spinel structure (JCPDS 47–0254) exhibited characteristic diffraction peaks at 2θ = 36.0°, 38.3°, 45.8°, and 53.7°. This stable spinel structure inhibited the chemical interactions between CuO and $Al_2O_3$, thereby improving the dispersion of CuO and preventing the growth of CuO crystals at high temperatures.

The $N_2$ adsorption–desorption isotherms and pore size distribution curves of the CuO–$Bi_2O_3$/$MgAl_2O_4$ catalysts under different conditions are shown in Fig. 2. The parameters of the surface structural characterization of the catalysts with varying MgO contents and calcination temperatures are listed in Table 1. As shown in Fig. 2a and c, the isotherms for this series of catalysts are concave without an inflection point. There is no clear saturated adsorption platform, and the high-pressure closure point of the hysteresis loop is near the right axis, which is characteristic of a V-type adsorption isotherm and H3-type hysteresis loop. However, the shape of the hysteresis loop and $p/p_0$ position for each sample varied slightly, with the relative pressure of the isotherm mutation increasing with increasing MgO content (Fig. 2a), indicating an increase in the number of macropores on the catalyst surface. The sample calcined at 450 °C exhibited the largest hysteresis loop (Fig. 2c), number of micropores, and pore volume (Fig. 2d), indicating that 450 °C was the optimal calcination temperature.

As shown in Table 1, with increasing MgO content, the specific surface area of the catalyst significantly decreased, pore volume decreased, and pore size increased, which is consistent with previous findings [38,39]. The size of the CuO crystals increased with increasing MgO content in the catalyst, indicating that higher MgO content decreased the specific surface area and dispersion of CuO on the surface of the catalyst, resulting in partial CuO aggregation. The specific surface area and pore volume of the catalysts increased with increasing calcination temperatures from 250 °C to 450 °C; however, the pore diameter remained constant (Table 1). In the calcination temperature range of 450°C-650 °C, the specific surface area and pore volume of the catalyst decreased with increasing temperature, whereas the pore diameter slightly increased. The catalyst calcined at 450 °C exhibited the largest surface area and smallest size of the CuO crystals, as shown in Table 1, indicating that CuO calcined in this temperature range was better dispersed, thus exposing more active sites.

This phenomenon may be attributed to the fact that the $MgAl_2O_4$ phase did not form at low calcination temperatures (<375 °C), resulting in the aggregation of CuO crystals. At a calcination temperature of 650 °C, the particle size of CuO increased to 22.6 nm. As shown in Table 1, the trend in the size of CuO crystals with increasing calcination temperature indicates that the $MgAl_2O_4$ phase

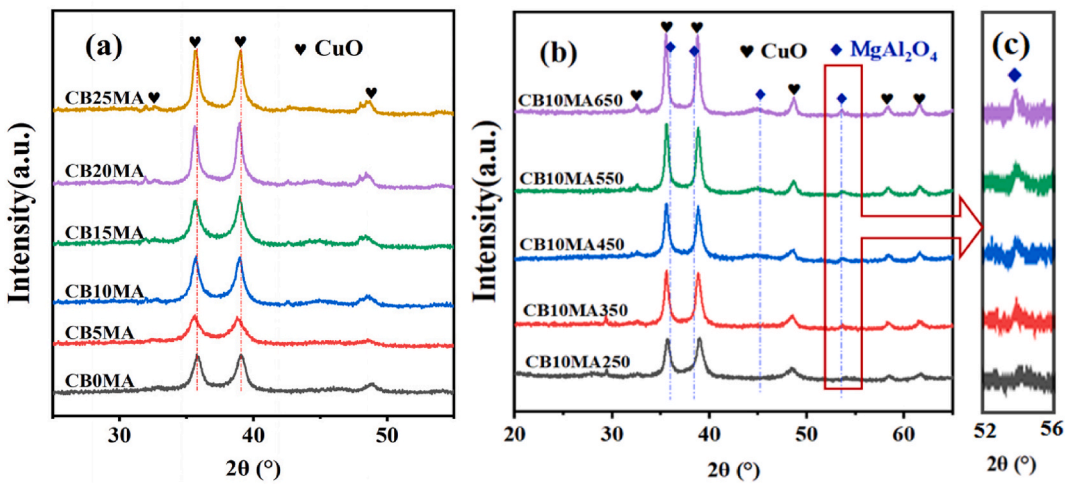


**Fig. 1.** X-ray diffraction patterns of the catalysts prepared under different conditions: varying (a) MgO contents and (b) calcination temperatures and (c) an enlarged view of the region marked in (b).

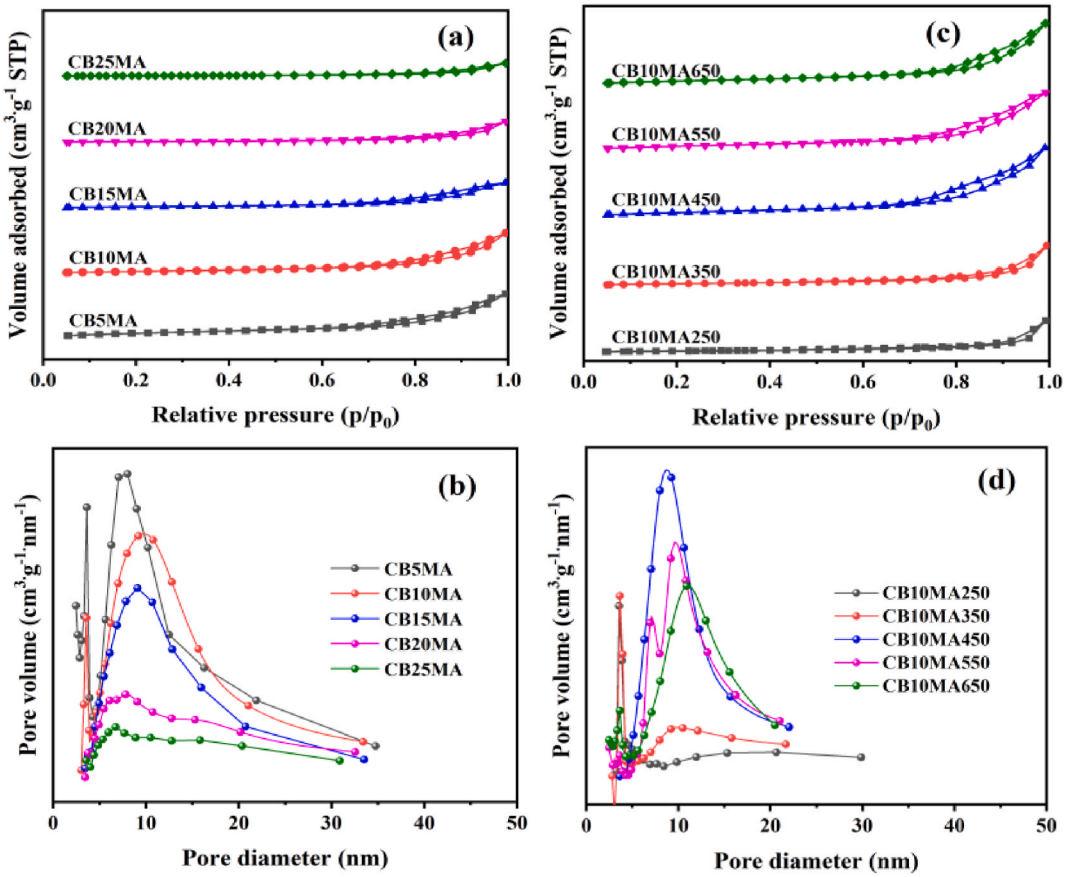


**Fig. 2.** $N_2$ adsorption–desorption isotherms and pore size distributions of the catalysts under different preparation conditions: varying (a) and (b) MgO contents and (c) and (d) calcination temperatures.

**Table 1**
Physical parameters of the catalysts with varying MgO contents and calcination temperatures.

| Samples | BET Area[a] ($m^2 \cdot g^{-1}$) | Pore Volume[b] ($cm^3 \cdot g^{-1}$) | $d_{pore}$[c] (nm) | $d_{CuO}$[d] (nm) |
|---|---|---|---|---|
| CB5MA | 100 | 0.327 | 8.81 | 10.3 |
| CB10MA | 83 | 0.313 | 11.85 | 15.5 |
| CB15MA | 33 | 0.126 | 13.79 | 15.8 |
| CB20MA | 20 | 0.103 | 15.22 | 16.5 |
| CB25MA | 13 | 0.065 | 14.60 | 19.2 |
| CB10MA250 | 32 | 0.157 | 11.48 | 16.3 |
| CB10MA350 | 43 | 0.198 | 11.51 | 18.0 |
| CB10MA450 | 83 | 0.313 | 11.85 | 15.5 |
| CB10MA550 | 78 | 0.292 | 12.74 | 16.8 |
| CB10MA650 | 74 | 0.278 | 13.24 | 22.6 |

[a] Specific surface area of the catalyst, calculated from the flat region of the Brunauer–Emett–Teller plot.
[b] Pore volume of the catalyst, estimated from the Barett–Joyner–Halenda isotherm.
[c] Pore diameter of the catalyst, estimated from the Barett-Joyner-Halenda isotherm.
[d] CuO crystal size, estimated using the Scherrer formula.

significantly inhibited the aggregation and growth of CuO crystals in the 450°C-550 °C range.

Fig. 3 shows the STEM images of the CB10MA450 catalyst. A lattice spacing of 0.235 nm (Fig. 3a) corresponds to the (111) crystal plane of the CuO crystals, as confirmed by the XRD data [40,41]. In addition, STEM-energy-dispersive X-ray spectroscopy was used to analyze the elemental distribution on the catalyst surface (Fig. 3b). Notably, Al was more densely distributed in regions with a dense Mg distribution. This finding indicates that basic MgO initially interacts with the acidic sites on $\gamma$-$Al_2O_3$ [42]. Subsequently, the $MgAl_2O_4$ phase formed, which weakened the interaction between Cu and Al in the support. This one-pot synthesis method improves

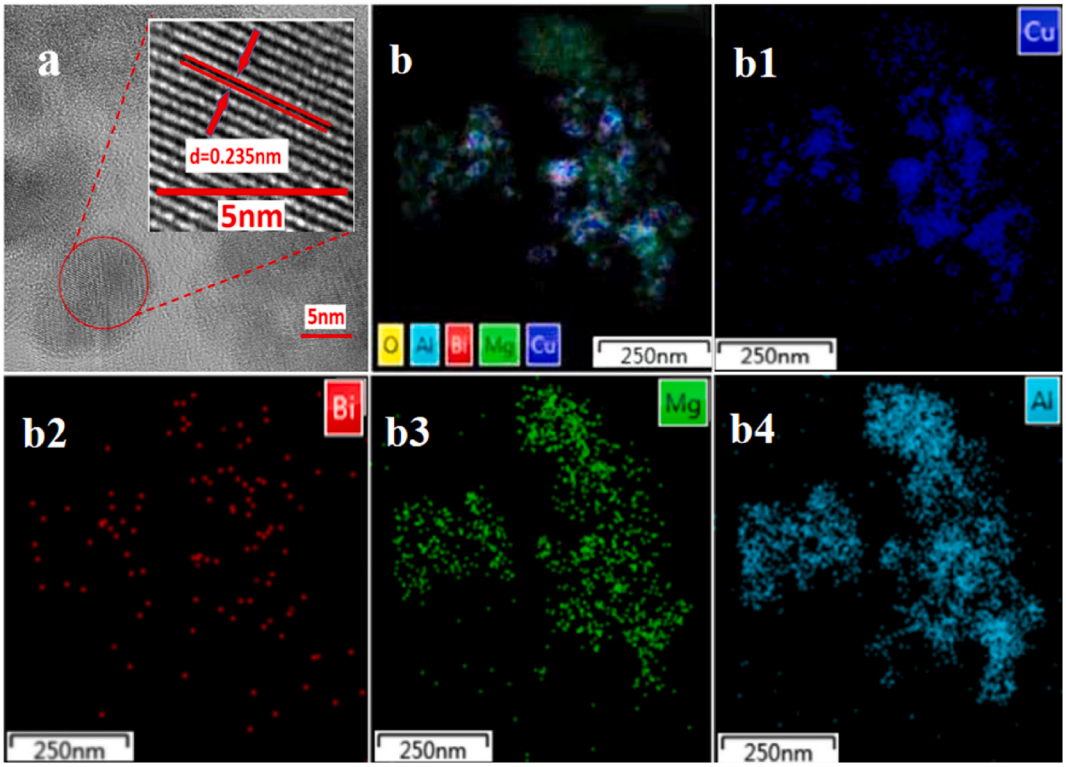


**Fig. 3.** Transmission electron microscopy (TEM) images of the CB10MA450 catalyst: (a) high-resolution TEM and (b) scanning TEM energy-dispersive X-ray spectroscopy images.

the surface acid–base properties of the catalyst, resulting in good reduction and activity and reduced formation of polyacetylene [16].

### 3.2. XPS analysis

To understand the valence states and chemical environments of Cu on the catalyst surface, we analyzed catalysts with varying surface Mg contents by XPS. The Cu 2p spectrum, as shown in Fig. 4a, indicates that all catalyst samples exhibited Cu 2p3/2, satellite, and Cu 2p1/2 peaks at 933.8, 942.0, and 953.7 eV, respectively. These observations indicate that the primary valence state of Cu is $Cu^{2+}$. Peak fitting of the characteristic Cu 2p3/2 peaks (Fig. 4b) revealed that Cu exists in two chemical states: one with a higher binding energy (935.02–936.11 eV) attributed to the interactions between $Cu^{2+}$ and Al–O, Mg–O, and Bi–O [43–45]. and another with a lower binding energy (933.7–934.68 eV) attributed to the free state of CuO.

The Cu contents in different chemical states are listed in Table 2. Typically, the binding energy of Mg 1s ranges from 1303.00 to 1303.90 eV [46]. With the introduction of MgO into the system, the binding energy of Mg 1s shifted slightly to 1304.20–1304.60 eV.

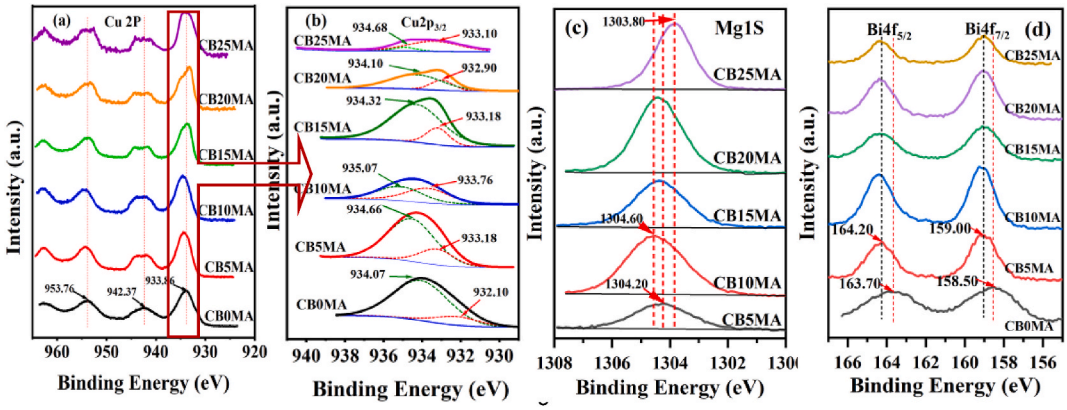


**Fig. 4.** X-ray photoelectron spectroscopy (XPS) spectra of catalysts with varying MgO contents: (a) Cu 2p, (b) Cu $2p_{3/2}$, (c) Mg 1s, and (d) Bi 4f.

This shift indicates the formation of the spinel $MgAl_2O_4$ phase [48]. The binding energy of Mg 1s increased with increasing MgO content, and the highest binding energy was 1304.60 eV at an MgO content of 10 % (Fig. 4c). Simultaneously, the free CuO content was the highest (Table 2), and the support contained $MgAl_2O_4$ and $Al_2O_3$. However, $Al_2O_3$ would fully reacted with MgO forming $MgAl_2O_4$ when the MgO content was ≥15 %. At this time $MgAl_2O_4$ and MgO were the main components in the support, and there was no chemical interaction between CuO and $Al_2O_3$. Meanwhile, the MgO caused CuO aggregation, increased crystals size, and decreased dispersibility. Consequently, the binding energy of Cu and Mg decreased and the free CuO decreased significantly.

The Bi $4f_{7/2}$ and Bi $4f_{5/2}$ peaks of CB5MA at 159.00 and 164.20 eV, respectively, correspond to the characteristic peaks of $Bi^{3+}$ (Fig. 4d) [47]. No peak shift was observed with increasing MgO content, indicating that Bi maintained a relatively stable chemical environment. Stable Bi can effectively inhibit the further reduction of $Cu^{+}$ to $Cu^0$ because $Cu^0$ catalyzes the conversion of $C_2H_2$ to polyacetylene, thereby decreasing the catalyst activity [13].

### 3.3. $H_2$-TPR profiles

The $H_2$-TPR profiles of the catalysts with varying MgO contents are shown in Fig. 5a. Because the reduction of $Bi_2O_3$ is challenging to initiate below 500 °C, all reduction peaks for the catalyst, as shown in Fig. 5, originated from the reduction of CuO [49]. As the MgO content increased, the initial and maximum $H_2$ reduction temperatures of CuO on the catalysts increased. These results indicate that CuO on the catalyst surface was increasingly difficult to reduce with increasing MgO content. In addition, the $H_2$ reduction peaks broadened with increasing MgO content, implying the presence of CuO species with varying reduction capacities. This finding indicates that CuO interacted with the support as the MgO content increased, thereby making it more difficult to reduce. The XRD patterns, as shown in Fig. 1, indicate that the size of the CuO crystals increases with the increasing MgO content, particularly when the MgO content is ≥ 20 %. The CuO particles grew rapidly, leading to decreased dispersion and increased difficulty in reducing the Cu species. CB5MA was easily reduced, and its peak was more symmetrical without broadening, indicating that the Cu species on the surface of the catalyst were primarily well dispersed and small. The interaction between Cu and the support was weak, facilitating the reduction of $Cu^{2+}$ to $Cu^0$ and resulting in decreased catalytic activity [13].

The $H_2$-TPR profiles of the CB10MA catalysts calcined at different temperatures are shown in Fig. 5b. The reduction temperature of CuO on the CB10MA catalyst increased with increasing calcination temperature. However, there was a minimal change in the reduction temperature when the calcination temperature exceeded 350 °C because $MgAl_2O_4$ began to form at this temperature, which inhibited the growth and aggregation of CuO particles. In the 400°C-550 °C range, the particle size and reduction temperature did not significantly change (Fig. 5c). These results indicate that the generated $MgAl_2O_4$ phase regulated the CuO reduction capacity. At 650 °C, the spinel $MgAl_2O_4$ phase completely formed, leading to the migration of CuO to the surface, which caused the dispersed CuO to aggregate and grow and led to an increase in the reduction temperature. An appropriate interaction between CuO and the support facilitates the moderate reduction of $Cu^{2+}$ to $Cu^{+}$ and formation of abundant active $Cu_2C_2$ centers during the ethynylation reaction. However, if CuO interacts with the support or the particle size is too large, the reduction of $Cu^{2+}$ to $Cu^{+}$ is difficult, which decreases the catalytic activity.

### 3.4. Acid–base properties of the catalyst surface

Fig. 6 shows the $CO_2$-TPD and $NH_3$-TPD profiles of the catalysts with varying MgO contents. All samples exhibited broad $CO_2$ desorption peaks in the 55°C-300 °C range, indicating the presence of basic sites with different strengths (Fig. 6a). The peaks at low temperatures were attributed to weakly basic sites (Peak1 and Peak3), indicating the presence of surface hydroxyl (–OH) groups. The $CO_2$ desorption peaks at high temperatures were attributed to moderate basic sites (Peak2 and Peak4), indicating interactions between metal–oxygen pairs (e.g., Mg–O and Al–O) [50]. Thus, the interaction between Mg-O and Al-O increased with increasing MgO content. As shown in $NH_3$-TPD profiles (Fig. 6b), the catalysts with varying MgO contents exhibited strong acidic sites at >300 °C. The shape of the $NH_3$ desorption peaks in the mid- and high-temperature zones broadened with increasing MgO content, indicating a clear trend toward multiple peaks and the existence of moderate and strong acidic sites with different strengths.

The $CO_2$-TPD and $NH_3$-TPD profiles of the CB10MA catalysts calcined at different temperatures are shown in Fig. 7. No significant effect on weak basic sites (Peak1) was observed at <250 °C. The $CO_2$ desorption peaks of the catalyst broadened in the 450°C-650 °C range, indicating an increase in the number of basic sites with different strengths (Peak2). At <350 °C, no $CO_2$ desorption peaks or low $CO_2$ contents were observed in the $CO_2$-TPD profile of CB10MA350. These results can be attributed to the formation of MgO owing to the decomposition of $Mg(OH)_2$ in the catalyst precursor at this temperature. Similarly, the number of strongly basic sites was higher at 250 °C because $MgAl_2O_4$ was not formed and Mg primarily existed as $Mg(OH)_2$ in the catalyst. Based on the BET data presented in Table 1, the catalysts calcined in the 450°C-550 °C range exhibited the largest specific surface area and smallest size of CuO crystals,

**Table 2**
Results of XPS analysis of catalysts with varying MgO contents.

| Samples | Cu $2p_{3/2}$ | |
|---|---|---|
| | Cu–O (%) | Cu–O–(Mg, Al) (%) |
| CB5MA | 20.22 | 79.78 |
| CB10MA | 49.55 | 50.45 |
| CB15MA | 17.27 | 82.73 |

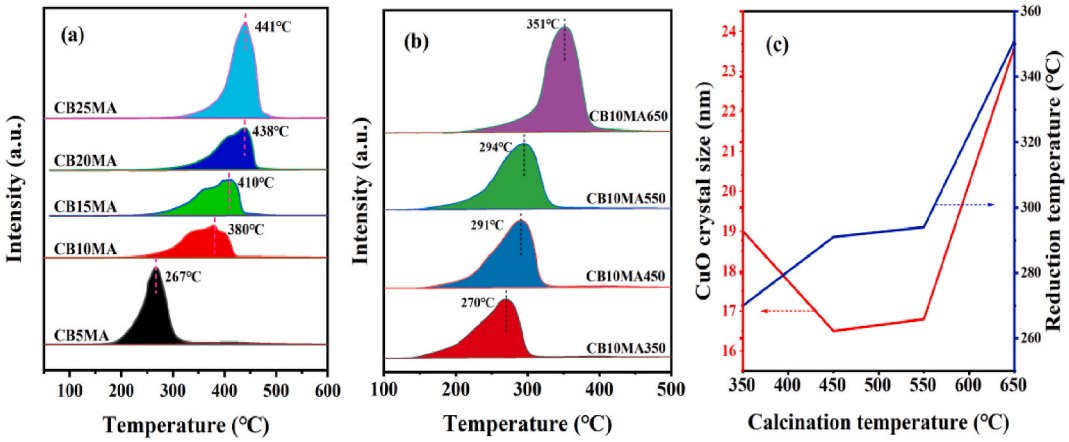


**Fig. 5.** Hydrogen temperature–programmed reduction profiles of the catalysts with varying (a) MgO contents and (b) calcination temperatures. (c) Size and reduction temperature of CuO crystals as a function of calcination temperature.

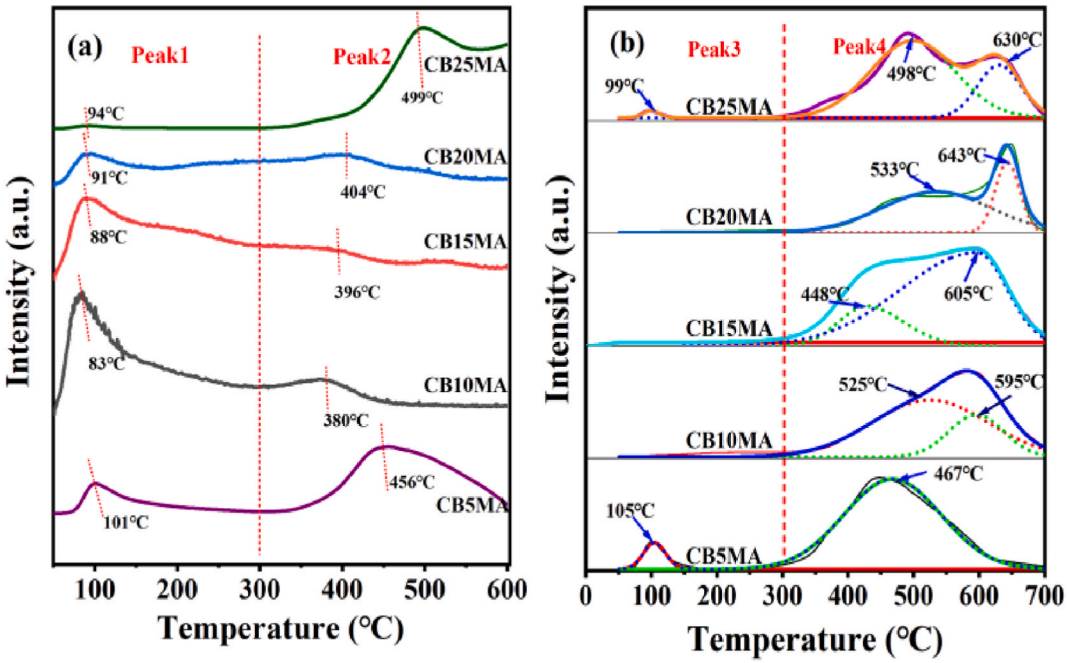


**Fig. 6.** Acid–base properties of the catalysts with varying MgO contents: (a) $CO_2$ temperature–programmed desorption (TPD) and (b) $NH_3$-TPD profiles.

indicating that CuO calcined in this temperature range could exhibit better catalytic performance. In addition, as indicated by the XRD patterns (Fig. 1b), $MgAl_2O_4$ was generated at 450 °C, and further formation of metal–oxygen pairs could lead to an increase in the number of moderate basic sites. Fig. 7b shows less intense $NH_3$ desorption peaks after calcination in the 50°C-175 °C range, corresponding to weak acidic sites (Peak3). As the temperature increased, the samples exhibited a broadening of $NH_3$ desorption peaks in the mid-to high-temperature regions, indicating the presence of medium–strong acidic sites with different properties (Peak 4).

The areas of the $CO_2$/$NH_3$-TPD desorption peaks, as shown in Figs. 6 and 7, were normalized using the normalization method, and the numbers of basic and acidic sites on the catalyst surface were calculated based on the $CO_2$/$NH_3$ fluxes, as listed in Table 3.

As shown in Table 3, the MgO content significantly affected the acid–base properties. The CB10MA catalyst containing 10 % MgO exhibited the fewest strongly basic and acidic sites but a moderate total number of basic and acidic sites. The number of acidic and basic sites on the catalyst surface initially decreased but then increased with increasing calcination temperature. The CB10MA450 catalyst exhibited a higher number of weakly basic sites and lowest amounts of strongly basic and acidic sites, which enhanced the catalysis of the ethynylation reaction. MgO, a typical alkaline earth metal compound, exhibits a diverse range of basic sites on its surface, and its addition significantly influences the acid–base properties of the support surface. The calcination temperature also

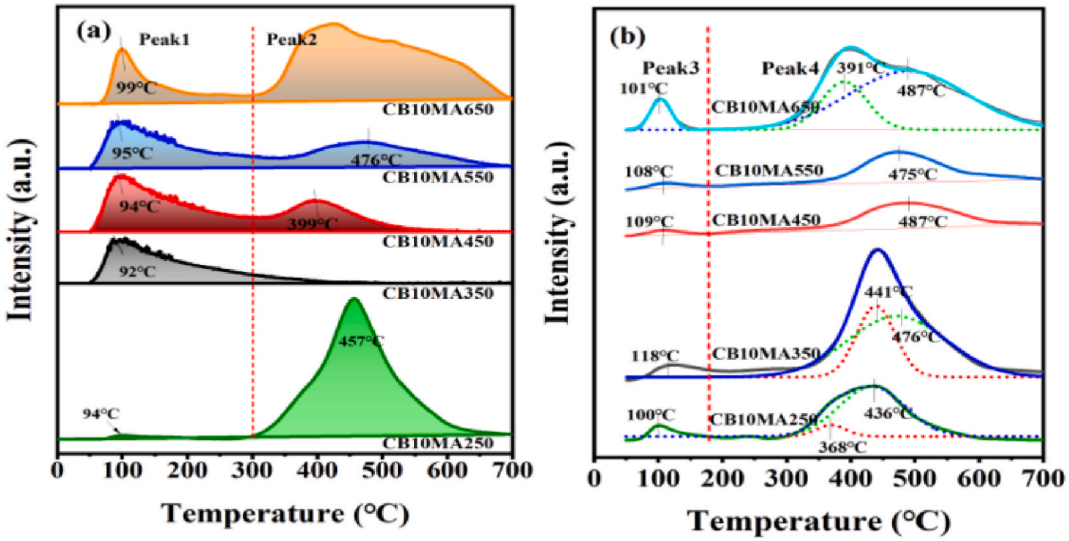


**Fig. 7.** Acid–base properties of the CB10MA catalysts at different calcination temperatures: (a) $CO_2$-TPD and (b) $NH_3$-TPD profiles.

**Table 3**
Acidic and basic site contents in the catalysts prepared with varying MgO contents and calcination temperatures.

| Samples | Basic sites (mmol$CO_2$/g) | | | Acid sites (mmol$NH_3$/g) | | |
|---|---|---|---|---|---|---|
| | Peak 1 | Peak 2 | $B_{(OH)}$ | Peak 3 | Peak 4 | $A_{(H)}$ |
| CB5MA | 0.289 | 3.449 | 3.638 | 0.501 | 6.255 | 6.756 |
| CB10MA | 0.186 | 0.031 | 0.214 | 0.260 | 4.164 | 4.424 |
| CB15MA | 0.183 | 0.057 | 0.240 | 0.147 | 4.681 | 4.828 |
| CB20MA | 0.103 | 0.051 | 0.154 | 0.177 | 5.960 | 6.137 |
| CB25MA | 0.079 | 7.717 | 7.796 | 0.429 | 15.755 | 16.184 |
| CB10MA250 | 0.132 | 7.034 | 7.156 | 1.264 | 11.624 | 12.888 |
| CB10MA350 | 0.152 | – | 0.152 | 0.289 | 2.690 | 2.979 |
| CB10MA450 | 0.181 | 0.110 | 0.291 | 0.070 | 1.224 | 1.294 |
| CB10MA550 | 0.165 | 0.148 | 0.313 | 0.077 | 1.257 | 1.334 |
| CB10MA650 | 0.498 | 2.222 | 2.720 | 0.365 | 4.517 | 4.882 |

affects the chemical state of MgO in the catalyst, which influences its catalytic performance [51,52].

### 3.5. Catalytic performance in the ethynylation reaction

#### 3.5.1. Effect of preparation conditions on catalytic activity

Fig. 8 shows the activity of the catalysts prepared under different conditions. The activities of the catalysts prepared using CB0MA, MgO (CBM0A), and CB10MA as supports are shown in Fig. 8a. The conversion followed the order CB10MA > CBM0A > CB0MA, whereas the selectivity followed the order CB10MA > CB0MA > CBM0A. The activity of the catalysts supported on $MgAl_2O_4$ was significantly better than that of the catalysts supported on the other two supports. Moreover, the selectivity of the catalyst supported on MgO was extremely low, which can be attributed to the dissolution of MgO in the acidic reaction mixture, resulting in severe damage to the structure of the catalyst. This structural damage significantly influences the separation of catalysts from the mixture in the slurry bed reactor.

Fig. 8b shows the activity data for the C10MA, CF10MA, and CB10MA catalysts. CB10MA exhibited the highest activity. However, the CF10MA catalysts, in which Fe was substituted for Bi, exhibited slightly lower activity than the CB10MA catalyst. Wang et al. [53] prepared catalysts with Cu and Cu–Fe as the active components on $SiO_2$–MgO support. The catalyst with Cu–Fe as the active component was more active than the catalyst with Cu as the active component in the ethynylation reaction.

Fig. 8c shows that the conversion was significantly influenced by the MgO content. It gradually increased with increasing MgO content and stabilized at approximately 97 % when 10 % MgO was added. The selectivity for the product (BYD) increased with increasing MgO content, and a maximum selectivity of approximately 80 % was achieved. The BYD yield was the highest under these conditions.

The activity data of CB10MA after calcination are shown in Fig. 8d. With increasing temperature, the activity of the CB10MA catalyst initially increased and then decreased, with the lowest activity observed at 350 °C and the highest at 450 °C. Considering all the characterization results, the primary reason for the low activity at 350 °C can be attributed to the significant aggregation of CuO

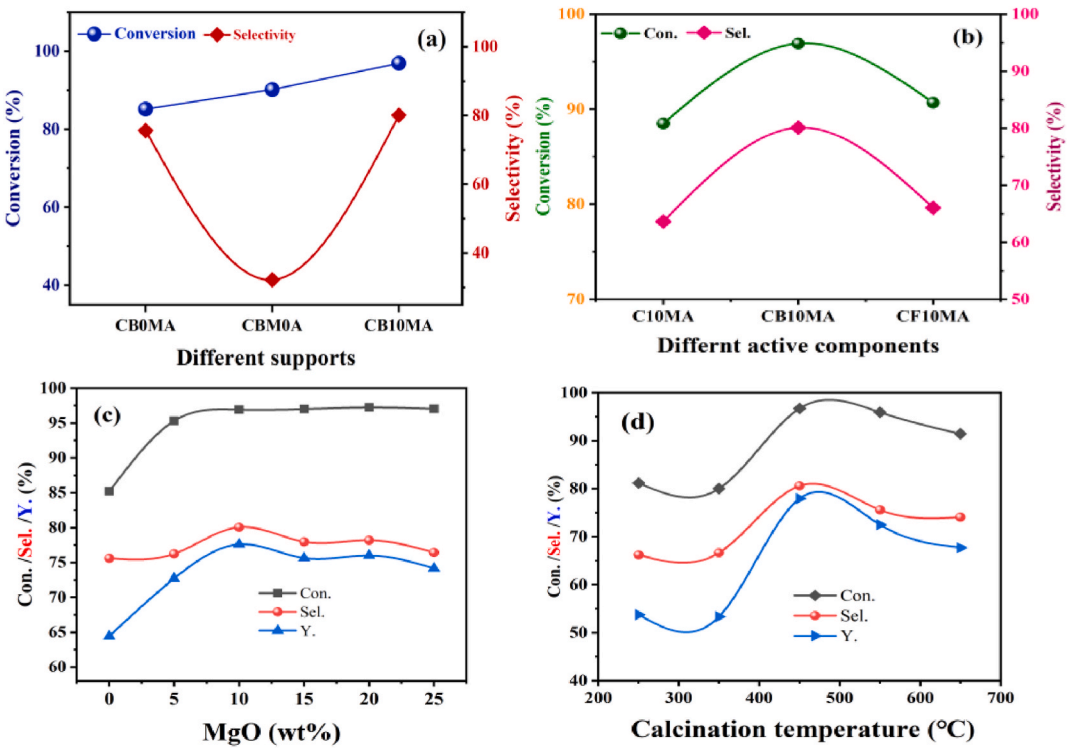


**Fig. 8.** Effects of the preparation conditions on the catalytic activity: (a) support, (b) promoter, (c) MgO content, and (d) calcination temperature.

crystals on the catalyst surface, which resulted in larger particle sizes. In addition, $MgAl_2O_4$ had not yet formed, resulting in the interaction between the CuO and Mg- and Al-containing phases in the support. As previously described, the CB10MA catalyst formed the $MgAl_2O_4$ support, facilitating the optimal interaction between CuO and the support, and enabling CuO to effectively participate in the reduction reaction. Therefore, the structure–activity relationship of the catalysts after calcination at 450 °C was the most favorable.

### *3.5.2. Influence of acid–base type and strength on the catalyst structure and activity*

Among the three supports (Fig. 8a), MgO exhibited the strongest alkalinity. Although the alkalinity of the catalyst enhances the HCHO conversion, it does not significantly affect the BYD selectivity. The $Al_2O_3$ support introduces more acidic sites on the catalyst [16], which is undesirable for catalytic conversion, as previously discussed. MgO and $Al_2O_3$ combined to form the $MgAl_2O_4$ support with suitable surface acid strength. Thus, the acid strength followed the order MgO < $MgAl_2O_4$ < $Al_2O_3$ [54,55]. Because the HCHO solution is inherently acidic, a moderate number of weak basic sites facilitate the HCHO ethynylation reaction. However, numerous acidic sites hinder the adsorption of acidic reactants. The CB10MA catalyst with 10 % MgO exhibited suitable basic and acidic sites, which facilitated the ethynylation reaction. Furthermore, CB10MA450 exhibited large surface area, pore volume, and pore size, which facilitated the reaction.

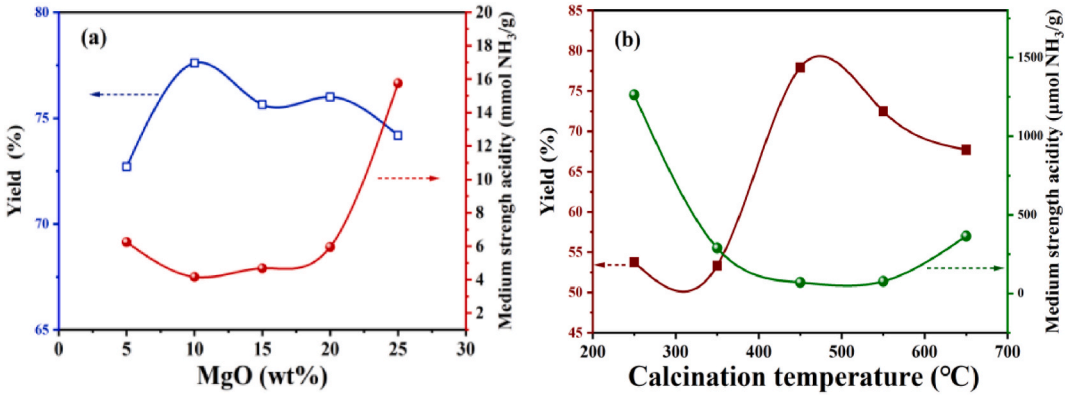


**Fig. 9.** Correlation between catalytic activity and acidity type and strength: Effect of (a) MgO content and (b) calcination temperatures.

$CO_2$/$NH_3$-TPD analysis revealed that both the MgO content and calcination temperature influenced the acid–base properties of the catalyst surface. The correlation between the amount of acid and base on the catalyst surface and catalyst activity is shown in Fig. 9. As shown in Fig. 9a, the amount of moderate acidic sites on the surface of the catalyst initially decreased as the MgO content increased and then increased when the MgO content reached 10 %. Wang reported that the incorporation of MgO into the catalyst enhanced the basic sites, which improved the activity and stability of the catalyst [27]. This correlation was also observed at different calcination temperatures in this study, as shown in Fig. 9b. Therefore, the number of moderate acidic sites on the catalyst was detrimental to its activity. Furthermore, the increase in the calcination temperature and increase in the number of metal–oxygen pairs resulted in moderately strong basic sites [44].

### 3.5.3. Effects of reaction conditions on the activity

Fig. 10 shows the activity of the CB10MA450 catalyst at 70 °C, 80 °C, and 90 °C. The conversion was significantly influenced by the reaction time and temperature, as shown in Fig. 10a. Tamhankar investigated the kinetics of the reaction between $C_2H_2$ and CuO to form $Cu_2C_2$. The reaction significantly depended on temperature, with a significant contribution of gas–liquid mass transfer at higher temperatures [56]. The adsorption of HCHO is crucial for controlling the ethynylation reaction, and the product BYD is also adsorbed [57]. Thus, lower HCHO and higher BYD contents were observed, and a further increase in the reaction time resulted in a limited increase in the conversion rate. As shown in Fig. 10b, the yield of BYD was significantly affected by the reaction time and temperature. Ethynylation is an exothermic reaction, and high temperatures are thermodynamically unfavorable for the reaction; however, an appropriate increase in the temperature of the slurry bed is beneficial to the reaction kinetics.

Fig. 10c shows that the pH of the solution also significantly affected the activity, with an optimal pH range for the ethynylation reaction. When the solution pH was too low (4–4.5), the catalyst broke and pore size distribution was significantly altered. This phenomenon led to a decrease in the content of active intermediate $Cu_2C_2$ and an increase in the linear carbon content, particularly β-type linear carbon, which is detrimental to the catalytic reaction [19]. In the pH range of 5.5–6, the catalyst exhibited optimal activity. Further increase in the pH significantly affected the selectivity and increased the concentration of alkali-metal ions in BYD, which was detrimental to its purification.

### 3.5.4. Catalytic activity and stability

The performance of the catalyst was evaluated through the continuous testing of its activity and stability, and the results are shown in Fig. 11. The CB10MA catalyst exhibited high conversion and stability without a significant decline after eight cycles. In addition, the leaching of Cu from the BYD after each reaction, as measured by ICP, was less than 0.7 mg/L.

The activity and stability of similar reported catalytic systems are presented in Table 4. The catalysts synthesized in this study exhibited superior activity and stability.

## 3.6. Effect of support $MgAl_2O_4$ and the mechanism of ethynylation

The ethynylation of HCHO appears to be a homogeneous reaction; however, it is a pseudo-homogeneous reaction, that is, a heterogeneous reaction. The bimolecular catalytic reaction on solid catalysts follows the Langmuir–Hinshelwood (L–H) mechanism, as reported in the literature (Scheme 1) [11].

In this study, a Cu–Bi/$MgAl_2O_4$ catalyst was synthesized via the one-pot coprecipitation of $Cu^{2+}$ $Bi^{3+}$, $Mg^{2+}$, and $Al^{3+}$ ions instead of a conventional impregnation method using solid $MgAl_2O_4$ as a support. Previous studies reported that the impregnation method was used to prepare a supported Cu–Bi catalyst using γ-$Al_2O_3$ and other supports; however, the catalytic activity of these catalysts was poor [28]. $Mg^{2+}$ can fill the vacancies in the oxygen tetrahedral lattice and form a surface layer of spinel $MgAl_2O_4$ when it is incorporated into γ-$Al_2O_3$ [58]. This phase structure is extremely stable and provides a suitable acid–base environment, facilitating the dispersion of CuO and $Bi_2O_3$.

Fig. 8a demonstrates that the catalyst supported on $MgAl_2O_4$ exhibits superior catalytic activity and structural stability compared with the conventional MgO@γ–$Al_2O_3$-supported Cu–Bi catalyst for the ethynylation reaction. The $CO_2$/$NH_3$-TPD analysis data presented in Fig. 9 indicate that as the MgO content increased, the number of the strong acidic sites on the catalyst surface initially decreased but then increased. However, the activity of the catalyst decreased with the increasing amount of acidic sites. The XPS data revealed that the chemical state of $Bi^{3+}$ was highly stable, indicating that the adsorption of $Cu^{+}$ and $Bi^{3+}$ by –OH on the surface of $MgAl_2O_4$ resulted in an interfacial effect. The alkaline Mg ions in the support facilitated the adsorption of $CH_2O$ in a weakly acidic environment, thereby enhancing the accessibility of adsorbed activated $C_2H_2$ and HCHO, reducing steric hindrance, and promoting the reaction rate. The XRD analysis revealed the absence of Cu aluminate phase in the sample, indicating that the Mg–O–Al structure effectively prevented the interaction between $Cu^{2+}$ and the –OH groups on the catalyst surface, thereby preventing the formation of the $CuAl_2O_4$ phase. The XPS, TEM, and SEM analyses indicated that $MgAl_2O_4$ improved the dispersion of $Cu^{2+}$ and $Bi^{3+}$. The high dispersion of CuO facilitated cooperation with moderately strong basic sites and improved the reduction of $Cu^{2+}$ to $Cu^{+}$. Based on the $H_2$-TPR characterization results, $Cu^{2+}$ exhibited the most appropriate interaction with $MgAl_2O_4$. When the MgO content was <10 %, $Cu^{2+}$ was easily reduced; however, the catalytic activity was poor, indicating that $Cu^{+}$ is further reduced to $Cu^{0}$ during the reaction. This synergistic effect effectively prevented $Cu^{0}$ from catalyzing the Glaser reaction of $C_2H_2$, as reported in the literature [17,19,22,58].

During the ethynylation reaction, HCHO initially undergoes diffusion and adsorption onto the surface of the catalyst, where $Cu^{2+}$ is reduced to $Cu^{+}$. The subsequent reaction of $C_2H_2$ with $Cu^{+}$ yields $Cu_2C_2$, which acts an active intermediate in the ethynylation reaction occurring at the active $Cu^{+}$ sites [18,58,59]. Each Cu atom forms π-bonds with at least two $C_2H_2$ groups. The structure of $Cu_2C_2$ on the

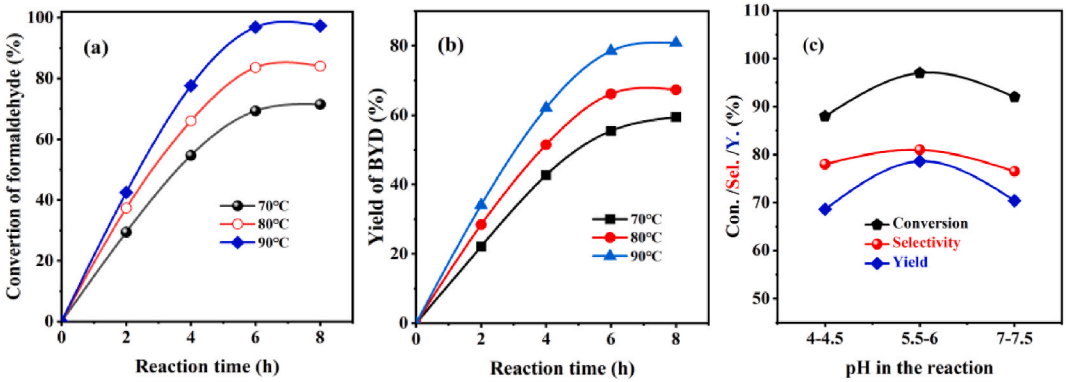


**Fig. 10.** Effect of reaction conditions on the performance of the CB10MA450 catalyst: (a) conversion at different temperatures as a function of reaction time, (b) yield at different temperatures as a function of reaction time, (c) activity as a function of pH.

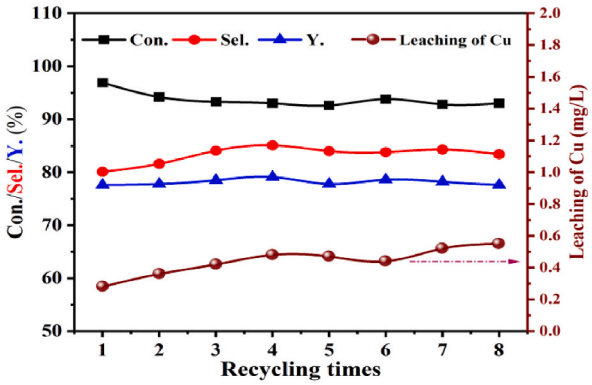


**Fig. 11.** Catalytic activity and stability.

**Table 4**
Activity and stability of reported catalysts for the ethynylation reaction.

| Catalysts | Reaction conditions | Conversion (%) | Yield (%) | Stability | ref. |
|---|---|---|---|---|---|
| CuO–ZnO/$SiO_2$ | 1.2 g catalyst, 20 mL 20 % $CH_2O$, 75 °C, and 9 h + 90 °C 7 h | | 72 | The yield was 48 % after seven cycles | [16] |
| Cu–Bi/MCM-41 | 1.2 g catalyst, 20 mL 19 % $CH_2O$, 75 °C, and 9 h + 90 °C 7 h | 57 | 53 | | [25] |
| CuO/$SiO_2$–MgO | 0.5 g catalyst, 10 mL 28 % $CH_2O$, 90 °C, and 15 h | | 67 | | [27] |
| CuO–FeO/ $SiO_2$–MgO | 5 g catalyst, 100 mL $CH_2O$, 90 °C, and 10 h | 55 | 47 | | [53] |
| CuO–$Bi_2O_3$/ $MgAl_2O_4$ | 25 g catalyst, 300 mL 20 % $CH_2O$, 90 °C, and 6 h | 97 | 78 | The yield was 78 % after eight cycles | This study |

$$HCHO_{(s)} + C_2H_{2(s)} \rightarrow HC{\equiv}C{-}CH_2OH_{(s)} \quad (2)$$

$$HC{\equiv}C{-}CH_2OH_{(s)} + HCHO_{(s)} \leftrightarrows HOCH_2C{\equiv}C{-}CH_2OH_{(s)} \quad (3)$$

$$HOCH_2C{\equiv}C{-}CH_2OH_{(s)} \leftrightarrows HOCH_2C{\equiv}C{-}CH_2OH_{(aq)} \quad (4)$$

**Scheme 1.** Langmuir–Hinshelwood mechanism of formaldehyde (HCHO) ethynylation to form 1,4-butynediol [11].

catalyst is shown in Scheme 2 [60]. The abundant moderately basic sites on the catalyst surface facilitated the adsorption of HCHO. Simultaneously, $C_2H_2$ is nucleophilic toward $Cu^+$, and after adsorption on $Cu_2C_2$, it forms a coordination of $Cu_2C_2{\bullet}3C_2H_2$ and $Cu_2C_2{\bullet}H_2O{\bullet}n\ C_2H_2$ with many $C_2H_2$ molecules [18,58].

The $H^+$ in $C_2H_2$, which is activated by the $Cu^+$ nucleophile, attacks the activated C=O bond in HCHO to form propargyl alcohol

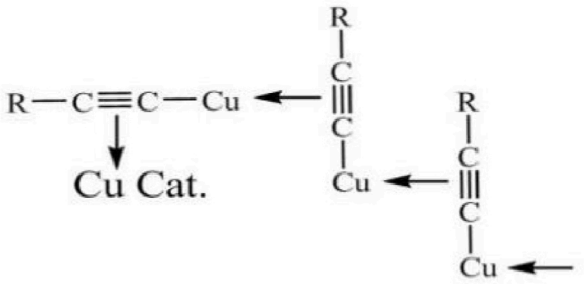


**Scheme 2.** Structure of the cuprous acetylide complex on the catalyst [18,60].

[17], which coordinates with $Cu_2C_2$ [61]. Owing to the high adsorption energy of propargyl alcohol on $Cu_2C_2$@$MgAl_2O_4$, the $C^+$ in the activated HCHO adsorbed on the basic sites on the support continues to attack the $C^-$ ion at the end of the alkynyl group in the adsorbed propargyl alcohol to form C–C bonds [59]. Reppe [61] found that propargyl alcohol readily reacted with HCHO to form BYD. The primary reactions are summarized in Scheme 3. The suitable moderate basic sites, pore volume, and pore size distribution on the $MgAl_2O_4$ support facilitated the timely desorption of BYD, ensuring that the catalyst maintained a high reaction rate, as demonstrated by the test data in Figs. 10 and 11. The adsorption energy of BYD on the catalyst was lower than that of propargyl alcohol, facilitating the desorption of BYD from the catalyst. This phenomenon enabled the remaining catalytic vacancies to enter the next cycle.

## 4. Conclusions

CuO–$Bi_2O_3$/$MgAl_2O_4$ catalyst was synthesized via a facile one-pot coprecipitation method using Cu, Bi, Mg, and Al nitrates and NaOH solution. A new spinel $MgAl_2O_4$ phase was formed when the catalyst precursor was calcined at 450 °C. In particular, the one-pot synthesis of the catalyst support facilitated the homogenous distribution of each component and improved the surface acid–base properties of the catalyst. The formation of the spinel $MgAl_2O_4$ phase during calcination was crucial for achieving moderately strong acid–base characteristics. Strong acidity was unfavorable for catalyst activity. In addition, $MgAl_2O_4$ inhibited the aggregation and growth of CuO particles, enabling the reduction of $Cu^{2+}$ to active $Cu^+$ sites, resulting in enhanced activity and stability of the catalyst.

The MgO content and calcination temperature significantly affected the structure, surface acid–base properties, and catalytic activity. The catalytic performance evaluation indicated that 97 % conversion and 80 % selectivity were obtained after the online monitoring of the reaction for 6 h. In addition, the leaching of Cu in the solution, as determined by ICP analysis, was less than 0.7 mg/L, resulting in a longer catalyst lifetime in the recycling tests. Insights into the role of the valence states of $MgAl_2O_4$ in the catalytic system and synergistic interaction between the active $Cu^+$ species and basic sites on the $MgAl_2O_4$ surface can provide theoretical guidance for the rational design of catalysts, particularly for the one-pot synthesis of $MgAl_2O_4$ supports for pseudo-homogeneous reactions.

## Notes

The authors declare no competing financial interest.

## Data availability statement

The data that support the findings of this study are available on request from the corresponding author.

## CRediT authorship contribution statement

**Gang Guan:** Writing – original draft. **Fengyun Ma:** Supervision, Funding acquisition, Conceptualization. **Ping Luo:** Writing – review & editing, Funding acquisition, Conceptualization. **Xiaolin Zhang:** Software, Resources. **Xiaoding Li:** Writing – review &

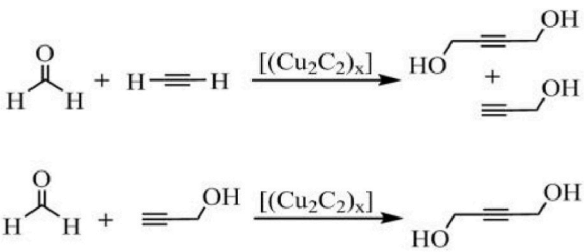


**Scheme 3.** Reactions during the catalytic ethynylation of HCHO [18].

editing, Methodology. **Guangxing Li:** Writing – review & editing, Supervision.

## Declaration of competing interest

The authors declare that they have no known competing financial interests or personal relationships that could have appeared to influence the work reported in this paper.

## Acknowledgements

The authors thank the Xinjiang Autonomous Region of China (2019AB011, 2021A01002-1) and the special funds for science and technology development in Hubei Province, China (P20501400006) for providing financial support. We also acknowledge the Key Laboratory of Catalysis and Materials Science of the State Ethnic Affairs Commission and the Ministry of Education, South-Central Minzu University for TEM and XRD analyses.

## Appendix A. Supplementary data

Supplementary data to this article can be found online at https://doi.org/10.1016/j.heliyon.2024.e38721.

## References

[1] P. Luo, X.D. Li, Application and market of 1,4-butanediol production of reppe method in China, Am. J. Chem. Eng. 9 (2021) 34–38, https://doi.org/10.11648/J.AJCHE.20210902.11.
[2] Y.D. Wang, C. Liu, H. Dong, Y.F. Chen, Insight into the mechanism of the key step for the production of 1,4-butanediol on Ni(111) surface: a DFT study, Mol. Catal. 524 (2022) 112335, https://doi.org/10.1016/j.mcat.2022.112335.
[3] A. Matsuda, F. Sato, Y. Yamada, S. Sato, Efficient production of 1,3-butadiene from 1,4-butanediol over $Y_2O_3$ catalyst prepared through hydrothermal aging, Bull. Chem. Soc. Jpn. 95 (2022) 506–512, https://doi.org/10.1246/bcsj.20210457.
[4] M. Zhang, H.A. Long, J. Lu, M.M. Zhang, Selective hydrogenation of 1,4-butynediol to 1,4-butenediol over platinum encapsulated in ZSM-48 with one-pot synthesis method, Fuel 327 (2022) 125201, https://doi.org/10.1016/j.fuel.2022.125201.
[5] X.L. Gao, W.L. Mo, F.Y. Ma, T. Noritatsu, H.L. Wu, X. Fan, Effects of a forming process on the properties and structure of raney®-Ni catalysts for the hydrogenation of 1,4-butenediol, RSC Adv. 10 (2020) 5516–5524, https://doi.org/10.1039/c9ra10200k.
[6] H.L. Wu, F.Y. Ma, Y.L. Wang, Y. Zeng, H. Wu, S.J. Yin, T. Mian, P.N. Tsubaki, Heteroatom promoted Ni/$Al_2O_3$ catalysts for highly efficient hydrogenation of 1,4-butynediol to 1,4-butenediol, Chem. Select. 5 (2020) 10072–10080, https://doi.org/10.1002/slct.202001967.
[7] X.L. Gao, W.L. Mo, F.Y. Ma, X. Fan, The influence of nickel loading on the structure and performance of Ni-$Al_2O_3$ catalyst for hydrogenation of 1,4-butynediol to produce 1,4-butenediol, New J. Chem. 44 (2020) 7683–7689, https://doi.org/10.1039/d0nj00350f.
[8] H.L. Wu, L.S. Guo, F.Y. Ma, Y.L. Wang, W.L. Mo, X. Fan, H.J. Li, Y.M. Yu, I. Mian, N. Tsubaki, Structure and surface characteristics of Fe promoted Ni/$Al_2O_3$ catalysts for hydrogenation of 1,4-butynediol to 1,4-butenediol in a slurry-bed reactor, Catal. Sci. Technol. 9 (2019) 6598–6605, https://doi.org/10.1039/c9cy01195a.
[9] Y. Zhu, J.M. Yang, F. Mei, X.H. Li, C. Zhao, Bio-based 1,4-butanediol and tetrahydrofuran synthesis: perspective, Green Chem. 24 (2022) 6450–6466, https://doi.org/10.1039/d2gc02271k.
[10] G.H. Yang, F. Gao, L. Yang, J. Wang, $MnO_x$ effect on the performance of Cu-based catalysts in ethynylation of formaldehyde for 1,4-butynediol synthesis, React, Kinet. Mech. Cat. 135 (2022) 2611–2627, https://doi.org/10.1007/s11144-022-02265-z.
[11] J.J. Chu, K.T. Li, I. Wang, Kinetics of the synthesis of 1,4-butynediol over a copper bismuth/magnesium silicate catalyst, Appl. Catal. A: Gen. 97 (1993) 123–132, https://doi.org/10.1016/0926-860X(93)80079-6.
[12] L.J. Ban, H.T. Li, Y. Zhang, R.F. Wu, X. Huang, J.H. Zhao, Y.X. Zhao, Importance of zinc oxide in Cu-based catalysts for the ethynylation of formaldehyde to 1,4-butynediol, J. Phys. Chem. C 125 (2021) 16536–16549, https://doi.org/10.1021/acs.jpcc.1c04886.
[13] J. Jiang, S. Lin, C.L. Liu, Preparation and catalytic properties of nano-sized CuO/$Bi_2O_3$ powders, J. Syn. Chem 13 (2005) 45–48, https://doi.org/10.3969/j.issn.1005-1511.2005.01.010 (In Chinese).
[14] J.Y. Wang, Y. Jiang, J.C. Xie, J.H. Chen, X.X. Zhang, W. Jiang, Synthesis of 1,4-butanediol catalyzed by malachite, J. Syn. Chem 9 (2010) 26–29, https://doi.org/10.3969/j.issn.1005-1511.2010.z1.004 (In Chinese).
[15] Y.H. Zhou, G.W. Wu, H. Wu, L. Zhao, L. Lv, B.Q. Li, CuO-$Bi_2O_3$ catalyzes the synthesis of 1,4-butynediol, Mod. Chem. Ind. 32 (2012) 65–68, https://doi.org/10.16606/j.cnki.issn0253-4320.2012.12.020 (In Chinese).
[16] G.H. Yang, L.X. Yang, J.L. Chen, Effective performance of the Cu/Zn/$SiO_2$ catalyst applied in the ethynylation of formaldehyde for 1,4-butynediol synthesis, Ind. Eng. Chem. Res. 62 (2023) 21067–21077, https://doi.org/10.1021/acs.iecr.3c02424.
[17] Z.P. Wang, Z.Z. Niu, Q. Hao, L.J. Ban, H.T. Li, Y. Zhao, Z. Jiang, Enhancing the ethynylation performance of CuO-$Bi_2O_3$ nanocatalysts by tuning Cu-Bi interactions and phase structus, J. Catal. 9 (2019) 35, https://doi.org/10.3390/catal9010035.
[18] T. Bruhm, A. Abram, J. Häusler, O. Thomys, K. Köhler, Walter reppe revival-identification and genesis of copper acetylides $Cu_2C_2$ as active species in ethynylation reactions, Chem. Eur J. 27 (2021) 1–7, https://doi.org/10.1002/chem.202101932.
[19] X. Hu, Q.F. Bo, L.J. Cheng, Z. Liu, S.L. Yuan, Y. Jiang, B. Zhang, Effect of pH value on catalytic performance of copper-based catalysts in reaction of acetylene with formaldehyde, Nat. Gas. Chem. Ind. 45 (2020) 29–33 (In Chinese).
[20] P.S. Gupte, B.P. Jadkar, V.R. Chaudhari, Kinetics of ethynylation of formaldehyde to butynediol, React. Kinet. Catal. Lett. 24 (1984) 173–177, https://doi.org/10.1007/BF02069623.
[21] H.T. Li, L.J. Ban, Z.P. Wang, P.F. Meng, Y. Zhang, R.F. Wu, Y.X. Zhao, Regulation of Cu species in CuO/$SiO_2$ and its structural evolution in ethynylation reaction, Nanomaterials 9 (2019), https://doi.org/10.3390/nano9060842, 842-842.
[22] G.H. Yang, F. Gao, L.X. Yang, The importance of copper-phyllosilicate formed in CuO/$SiO_2$ catalysts in the ethynylation of formaldehyde for 1,4-butynediol synthesis, React, Chem. Eng. 8 (2023) 881–890, https://doi.org/10.1039/d2re00514j.
[23] D. Wang, Z.F. He, Q.F. Bo, H. Chen, M.X. Tang, Preparation and catalytic activity of CuO-$Bi_2O_3$/$SiO_2$ catalyst, J. Syn. Chem 22 (2014) 246–249 (In Chinese).
[24] G.H. Yang, Y.B. Xu, X.T. Su, Y.H. Xie, C. Yang, Z.J. Dong, J.D. Wang, MCM-41 supported CuO/$Bi_2O_3$ nanoparticles as potential catalyst for 1,4-butynediol synthesis, Ceram. Int. 40 (2014) 3969–3973, https://doi.org/10.1016/j.ceramint.2013.08.044.
[25] G.H. Yang, Y.M. Yu, M.U. Tahir, S. Ahmad, X.T. Su, Y.H. Xie, J.D. Wang, Promotion effect of Bi species in Cu/Bi/MCM-41 catalysts for 1,4-butynediol synthesis by ethynylation of formaldehyde, React. Kinet. Mech. Catal. 127 (2019) 425–436, https://doi.org/10.1007/s11144-019-01561-5.

[26] Y. Zheng, Z.J. Sun, Y.J. Wang, H.T. Li, S.A. Wang, M. Luo, J.L. Zhao, Y.X. Zhao, Preparation and acetylene properties of CuO-$Bi_2O_3$/$SiO_2$-MgO catalysts, J. Mol. Catal. 26 (2012) 233–238 (In Chinese).

[27] Z.P. Wang, L.J. Ban, P.F. Meng, H.T. Li, Y.X. Zhao, Ethynylation of formaldehyde over CuO/$SiO_2$ catalysts modified by Mg species: effects of the existential states of Mg species, Nanomaterials 9 (2019) 1137, https://doi.org/10.3390/nano9081137.

[28] B.C. Xu, X.D. Ge, Q.W. Gu, Synthesis of l,4-butynediol by slurry bed under lower pressures I. study of acetylene catalyst with different carriers, J. East China Univ. Sci. Technol. 3 (1989) 272–276 (In Chinese).

[29] Q.F. Bo, D. Wang, B. Zhang, Z.F. He, Y. Jiang, Preparation of CuO-$Bi_2O_3$-MgO/γ-$Al_2O_3$ catalyst and its catalytic synthesis of 1, 4-butanediol, Nat. Gas. Chem. Ind. 40 (2015) 41–43, https://doi.org/10.3969/j.issn.2095-1132.2015.01.012 (In Chinese).

[30] S.F. Liu, W.C. Peng, J.S. Zhang, Y.B. Tong, J. Yuan, X.X. Qi, X.R. Yan, D.K. Sun, B. Dai, Mesoporous CuO/MgO synthesized by a homogeneous-hydrothermal method and its catalytic performance for the ethynylation reaction of formaldehyde, Energy Sources, Part A Recovery, Util. Environ. Eff. 40 (2018) 2327–2333, https://doi.org/10.1080/15567036.2018.1487484.

[31] X.D. Li, J.S. Chen, Y.H. Li, X.W. Lǔ, Y.H. Kong, Study on deactivation of potassium-promoted Co-Mo/$Al_2O_3$ water-gas shift catalyst, J. Nat. Gas Chem. 3 (1994) 295–305.

[32] B. Bernard, G. Edouard, P. Michel, Stabilization of alumina by addition of lanthanum, Appl. Catal. 75 (1991) 119–132, https://doi.org/10.1016/S0166-9834(00)83128-0.

[33] X.D. Li, Y.H. Li, X.W. Lǔ, J.S. Chen, Y.H. Kong, Study on deactivation of Co-Mo/MgO-$Al_2O_3$ sulfur-resistant catalyst for water-gas shift, J. Appl. Chem. 11 (1994) 58–62 (In Chinese).

[34] X.D. Li, Y.H. Li, X.W. Lǔ, J.S. Chen, Y.H. Kong, Study on deactivation of Co-Mo/MgO-$Al_2O_3$ sulfur-resistant catalyst for water-gas shift I. analysis on phase, specific surface and crushing strength of fresh and used catalysts, Nat. Gas. Chem. Ind. 18 (1993) 12–15 (In Chinese).

[35] J.J. Guo, H. Lou, H. Zhao, X.G. Wang, X.M. Zheng, Novel synthesis of high surface area $MgAl_2O_4$ spinel as catalyst support, Mater. Lett. 58 (2004) 1920–1923, https://doi.org/10.1016/j.matlet.2003.12.013.

[36] I. Ganesh, A review on magnesium aluminate ($MgAl_2O_4$) spinel: synthesis, processing and applications, Int. Mater. Rev. 58 (2013) 63–112, https://doi.org/10.1179/1743280412y.0000000001.

[37] V.K. Singh, R.K. Sinha, Low temperature synthesis of spine1 ($MgA1_2O_4$), Mater. Lett. 31 (1997) 281–285.

[38] Q.Y. Zhong, Z.M. Tian, Y.F. Tang, X.T. Zhang, X. Li, F.S. Tang, Preparation of sulfur-resistant conversion catalyst QCS-04, Qilu Petrochem. Technol. 18 (1998) 9–14 (In Chinese).

[39] D.M. Jiao, L.B. Wu, F.H. Cao, Effect of MgO on the properties of Co-Mo/$Al_2O_3$-MgO catalysts, Petrochemical Industry 41 (2012) 405–409 (In Chinese).

[40] S. Kim, Y. Lee, A. Gu, C. You, K. Oh, S. Lee, Y. Im, Synthesis of vertically conformal ZnO/CuO core-shell nanowire arrays by electrophoresis-assisted electroless deposition, J. Phys. Chem. C 118 (2014) 7377–7385, https://doi.org/10.1021/jp410293j.

[41] M.R. Yu, G. Suyambrakasam, R.J. Wu, M. Chavali, Performance evaluation of ZnO-CuO hetero junction solid state room temperature ethanol sensor, Mater. Res. Bull. 47 (2012) 1713–1718, https://doi.org/10.1016/j.materresbull.2012.03.046.

[42] H. Ren, C.H. Xu, H.Y. Zhao, Y.X. Wang, J. Liu, J.Y. Liu, Methanol synthesis from $CO_2$ hydrogenation over Cu/γ-$Al_2O_3$ catalysts modified by ZnO, $ZrO_2$ and MgO, J. Ind. Eng. Chem. 28 (2015) 261–267, https://doi.org/10.1016/j.jiec.2015.03.001.

[43] D.B.C.D. Venkata, Š.N. Strah, B. Likozar, Correlation between synthesis pH, structure and Cu/MgO/$Al_2O_3$ heterogeneous catalyst activity and selectivity in $CO_2$ hydrogenation to methanol, J. $CO_2$ Util. 28 (2018) 193, https://doi.org/10.1016/j.jcou.2018.09.002.

[44] F. Vila, G.M. López, M. Ojeda, J.L.G. Fierro, R. Mariscal, Glycerol hydrogenolysis to 1,2-propanediol with Cu/-$Al_2O_3$: effect of the activation process, Catal. Today 187 (2012) 122–128, https://doi.org/10.1016/j.cattod.2011.10.037.

[45] C.L. Chiang, K.S. Lin, H.W. Chuang, Direct synthesis of formic acid via $CO_2$ hydrogenation over Cu/ZnO/$Al_2O_3$ catalyst, J. Clean. Prod. 172 (2018) 1957–1977, https://doi.org/10.1016/j.jclepro.2017.11.229.

[46] H. Seyama, M. Soma, X-ray photoelectron spectroscopic study of montmorillonite containing exchangeable divalent cations, Journal of the Chemical Society, Faraday Transactions 1, Physical Chemistry in Condensed Phases 80 (1984) 237–248, https://doi.org/10.1039/f19848000237.

[47] G.H. Yang, Y.M. Yu, M.U. Tahir, S. Ahmad, X.T. Su, Y.H. Xie, J.D. Wang, Promotion effect of Bi species in Cu/Bi/MCM-41 catalysts for 1,4-butynediol synthesis by ethynylation of formaldehyde, React. Kinet. Mech. Catal. 127 (2019) 425–436, https://doi.org/10.1007/s11144-019-01561-5.

[48] D.E. Haycock, C.J. Nicholls, D.S. Urch, M.J. Webber, G. Wiech, The electronic structure of magnesium dialuminium tetraoxide (spinel) using X-ray emission and X-ray photoelectron spectroscopies, J. Chem. Soc. Dalton Trans. 12 (1978) 1785–1790, https://doi.org/10.1039/dt9780001785.

[49] Z.P. Wang, Synthesis of $Cu_xO$-$MO_y$ Binary Catalysts and its Ethynylation Performance, Shanxi University, 2019 (In Chinese).

[50] Y.X. Lian, H.F. Wang, W.P. Fang, Y.Q. Yang, Effect of calcination temperature on performance of Co-Mo/MgO-$Al_2O_3$ conversion catalyst, J. Catal. 30 (2009) 549–554 (In Chinese).

[51] X.X. Huang, Y. Men, J.G. Wang, W. An, Y.Q. Wang, Highly active and selective binary MgO-$SiO_2$ catalysts for the production of 1,3-butadiene from ethanol, Catal. Sci. Technol. 7 (2017) 168–180, https://doi.org/10.1039/c6cy02091g.

[52] C. Angelici, M.E.Z. Velthoen, B.M. Weckhuysen, P.C.A. Bruijnincx, Influence of acid-base properties on the Lebedev ethanol-to-butadiene process catalyzed by $SiO_2$-MgO materials, Catal. Sci. Technol. 5 (2015) 2869–2879, https://doi.org/10.1039/c5cy00200a.

[53] J.J. Wang, H.X. Zhang, H.T. Li, Z.Q. Ma, Z.P. Wang, J.Y. Guo, Y.X. Zhao, Effect of iron promoter on structure and catalytic performance of CuO/$SiO_2$-MgO catalyst for formaldehyde ethynylation, Ind. Catal. 23 (2015) 455–458 (In Chinese).

[54] X.Y. Liu, S.J. Wang, L.C. Guo, Study on out-layer Mg-Al spinel of alumina base I.phase structure, pore structure and surface acidity of out-layer Mg-Al spinel and state of supported Pd, J. Catal. 15 (1994) 1–7 (In Chinese).

[55] C. Morterra, G. Ghiotti, F. Boccuzi, S. Coluccia, An infrared spectroscopic investigation of the surface properties of magnesium aluminate spinel, J. Catal. 51 (1978) 299313, https://doi.org/10.1016/0021-9517(78)90268-3.

[56] S.S. Tamhankar, S.P. Gupte, R.V. Chaudhari, Kinetics of a non-catalytic slurry reaction: reaction of acetylene with cuprous oxide suspended in water, Chem. Eng. J. 22 (1981) 15–24, https://doi.org/10.1016/0300-9467(81)85002-2.

[57] S.S. Kale, R.V. Chaudharl, P.A. Ramachandran, Butynediol synthesis. A kinetic study, Ind. Eng. Chem. Prod. Res. Dev. 20 (1981) 309–315, https://doi.org/10.1021/i300002a015.

[58] W. Reppe, J. Liebigs, Äthinylierung I Schwermetallacetylide als Katalysatoren für die Äthinylierung, Ann. Chem. 596 (1955) 6–11.

[59] S. Nikolai, G. Francesca, S. Grigory, R. Frank, A.S.K. Hashmi, T. Schaub, Copper-catalysed synthesis of propargyl alcohol and derivatives from acetylene and other terminal alkynes, Adv. Synth. Catal. 364 (2022) 2227–2234, https://doi.org/10.1002/adsc.202200369.

[60] A.M. Sladkov, L.Y. Ukhin, Copper and silver acetylides in organic synthesis, Russ. Chem. Rev. 37 (1968) 748–763, https://doi.org/10.1070/rc1968v037n10abeh001701.

[61] W. Reppe, Äthinylierung III Umsetzung von Acetylen und seinen monosubstituierten Derivaten mit Carbonylverbindungen, Ann. Chem. 596 (1955) 25.